Pre-print Manuscript of Article:
Bridgelall, R., "Precision bounds of pavement distress localization with connected vehicle sensors," *Journal of Infrastructure Systems*, American Society of Civil Engineering, 21(3), pp. 1-7, 2014.

Precision bounds of pavement distress localization with connected vehicle sensors

Raj Bridgelall, Ph.D.[1]

Abstract

Continuous, network-wide monitoring of pavement performance will significantly reduce risks and provide an adequate volume of timely data to enable accurate maintenance forecasting. Unfortunately, transportation agencies can afford to monitor less than 4% of the nation's roads. Even so, agencies monitor their ride quality at most once annually because current methods are expensive and laborious. Distributed mobile sensing with connected vehicles and smartphones could provide a viable solution at much lower costs. However, such approaches lack models that improve with continuous, high-volume data flows. This research characterizes the precision bounds of the Road Impact Factor transform that aggregates voluminous data feeds from geo-position and inertial sensors in vehicles to locate potential road distress symptoms. Six case studies of known bump traversals reveal that vehicle suspension transient motion and sensor latencies are the dominant factors in position estimate errors and uncertainty levels. However, for a typical vehicle mix, the precision improves substantially as the number of traversals approaches 50.

CE Database subject headings: Deterioration; Forecasting; Intelligent transportation systems; Pavement management; Preservation; Probe instruments; Surface roughness; Vibration

---

[1]Assistant Professor of Transportation and Program Director, Center for Surface Mobility Applications & Real-Time Simulation environments (SMARTSe[SM]), Upper Great Plains Transportation Institute, North Dakota State University, P.O. Box 863676, Plano, TX 75086. Phone: 408-607-3214, E-mail: raj@bridgelall.com

Author Keywords: Connected vehicles; International Roughness Index; Potholes; Ride quality; Road Impact Factor; Smartphones

Introduction

Practitioners have long recognized that rough roads increase the cost of operating vehicles (Zaniewski and Butler 1985)(Park et al. 2007) and lead to repairs that are more expensive (AASHTO 2009). Studies have also linked road roughness to motion sickness (Griffin 1990) and higher crash rates (Swedish National Road and Transport Research Institute 2004). Unfortunately, transportation agencies can seldom afford to profile roads for defects more often than once a year. Even so, those assessments are limited to portions of the National Highway System for which the Federal Highway Administration (FHWA) requires annual reporting of the International Roughness Index (IRI) (HPMS 2012). Consequently, agencies miss important vulnerabilities such as frost heaves that appear and disappear between monitoring cycles. For unmonitored roads, many agencies rely on the public to report the location and type of defect such as potholes. Unfortunately, agencies often learn about these anomalies after they begin to cause chronic traffic jams or crashes because drivers suddenly reduce speed when attempting to maneuver around them (FHWA and Federal Transit Administration 2011).

To provide continuous, network-wide, lower-cost assessments, the author developed and validated a data- and signal-processing method called the Road Impact Factor (RIF) transform. The average RIF for a road segment is directly proportional to the IRI (Bridgelall 2014). However, unlike the IRI, the RIF results from a windowed energy transform capable of providing higher resolution localization of anomalies, which this research defines as rough spots, some of which are unexpected distress symptoms. Statistically, the precision of localizing the true position of anomalies increases as the volume of sensor readings increases. The RIF transform aggregates data from global positioning system (GPS) receivers and inertial sensors in regular vehicles and smartphones to report ride quality.

This study characterizes bounds in the precision with which the RIF transform can estimate the position of road features that produce roughness peaks. Error factors include variances from GPS location tagging, vehicle speed and suspension parameters, and sensor characteristics. This is the first study to characterize the RIF precision bounds. Related studies extract features from inertial sensors to identify potholes among other anomalies. Such studies are complementary to this one because they do not characterize the precision of the anomaly location methods used. Their reported feature extraction methods include fixed thresholds of the accelerometer signal's standard deviation (Eriksson et al. 2008), (Dawkins et al. 2011), (Chen, Zhang and Lu 2011), time-domain heuristics (Mohan, Padmanabhan and Ramjee 2008), wavelet transforms (Hesami and McManus 2009), and principle component analysis (Hautakangas and Nieminen 2011). With such signal processing methods, researchers demonstrated that it is possible to differentiate between potholes and other road features that produce localized signal roughness.

This organization of this paper is as follows: the next section reviews the RIF transform and its direct proportionality with the IRI. The fourth section introduces the average RIF as a position estimator, and the fifth section defines its error component variances. The sixth section describes the case study characterizing the error statistics, bounds in achievable precision, and the estimator's sensitivity to each error component. The final section summarizes and concludes the study.

Ride-Index Model

As derived in previous work by the author (Bridgelall 2014), the RIF transform, denoted $R_{\bar{v}}^{\Delta L}$, is the g-force per meter (g/m) experienced when traveling a road segment of length ΔL where

$$R_{\bar{v}}^{\Delta L} = \sqrt{\frac{1}{\Delta L} \int_{0}^{\Delta L/\bar{v}} \left| g_z(t) v(t) \right|^2 dt} \tag{1}$$

The average and instantaneous vehicle speeds are $\bar{v}$ and $v(t)$, respectively. The vertical acceleration signal from an on-board accelerometer is $g_z(t)$. Previous work (Bridgelall 2014) derived a proportionality constant κ_{RI} that is a ratio of the RIF and IRI impulse responses as follows:

$$\kappa_{RI} = \frac{RIF}{IRI} = \frac{\bar{v}\sqrt{\frac{1}{\Delta L}}\,\frac{\gamma_z}{g}\sqrt{\omega_{\mu s}\left(\zeta_{\mu s} + \frac{1}{4\zeta_{\mu s}}\right) + \rho_z^2 \omega_{\mu u}\left(\zeta_{\mu u} + \frac{1}{4\zeta_{\mu u}}\right)}}{\frac{1}{2}\left(\frac{1}{\omega_{Gs}\zeta_{Gs}} + \frac{1}{\omega_{Gu}\zeta_{Gu}}\right)^2 \frac{1}{\sqrt{\left(1-\zeta_{Gs}^2\right)\left(1-\zeta_{Gu}^2\right)}}} \tag{2}$$

The g-force unit g normalizes the sensor constant γ_z. The average sprung mass resonance frequencies for the typical vehicle and the IRI Golden Car parameters are $\omega_{\mu s}$ and ω_{Gs}, respectively. The corresponding unsprung mass frequencies are $\omega_{\mu u}$ and ω_{Gu} respectively. Similarly, for the typical vehicle and the Golden Car the average sprung mass damping ratios are $\zeta_{\mu s}$ and ζ_{Gs} respectively, and those of the unsprung mass are $\zeta_{\mu u}$ and ζ_{Gu} respectively. The parameter ρ_z is a function of the sensor attachment in the vehicle. The proportionality constant is measurable by assessing the IRI and the average RIF from traversing a fixed-length segment at an arbitrary average speed. The ratio of future RIF values obtained at the same average speed used to determine the IRI proportionality constant will estimate future IRI values if needed.

Adjusting the parameter ΔL identifies anomalies in the RIF data set at the desired spatial resolution. For example, Fig 1 plots the RIF from a smartphone data logger affixed to the dashboard of a sports utility vehicle (SUV), traversing a speed bump at 7 m·s^{-1}. The labels g_x, g_y, and g_z point to the lateral, longitudinal, and vertical accelerations respectively in units of g-forces. The g_z signal offset of approximately -1g comes from the earth's constant downward gravitational force. The graph artificially offsets the g_x signal by +1g for display clarity. A three-dimensional rotation transformation described in previous work (Bridgelall 2014) produces the resultant vertical resultant acceleration from the individual accelerometers axis for any sensor orientation.

The RIF peak is an estimate of the true position of the anomaly that produced the peak g-forces. For the single traversal shown in Fig 1, the true position of the bump's center is about five meters ahead of the RIF peak as indicated by the vertical marker ξ shown at 30 meters. The roughness position estimator improves steadily by adding traversals to a windowed ensemble average of their RIFs. The next sections derive models to characterize the estimator's accuracy and precision.

Peak position estimate

The position of a peak $\breve{\upsilon}_p$ in the ensemble average RIF is an estimate of the bump's true position υ_p were

$$\breve{\upsilon}_p = \upsilon_p + \Delta L + \bar{\varepsilon}_i + \bar{\varepsilon}_d + \bar{\varepsilon}_s + \bar{\varepsilon}_{GPS} \tag{3}$$

That is, the estimate $\breve{\upsilon}_p$ contains biases from the RIF transform's integration window ΔL and four additional offset factors. The latter four biases are from the average error of peak RIF position $\bar{\varepsilon}_i$ within the distance interpolation sub-interval, the average suspension system transient response distance $\bar{\varepsilon}_d$, the average longitudinal sensor position $\bar{\varepsilon}_s$, and the average GPS tag lag $\bar{\varepsilon}_{GPS}$ from operating system latencies.

The peak position estimator is the ensemble average RIF within spatial windows Δw starting at position x where

$$\overline{R}^{\Delta w}(x) = \frac{1}{N_T} \sum_{\rho=1}^{N_v} R_{[\rho]}^{\Delta w}(x) \tag{4}$$

$\overline{R}^{\Delta w}(x)$ is the ensemble average RIF across N_v traversals with indices ρ, within a specified speed band. This research recommends practically narrow speed bands such as those within 5% to 10% of the average speed for that segment.

Interpolation sub-interval

Within a traversal, the position of a RIF index is an integer multiple of the resolution window distance from a known geo-spatial position marker at the beginning of the traversal path. To accommodate GPS position update variances across traversals, the ensemble-averaging algorithm divides each window into higher resolution sub-intervals and interpolates the RIF within each. The length of each interpolation sub-interval is $\delta_v = \overline{v}\,\tau_A$ where the update interval for the accelerometer is τ_A. Hence, the error in estimating the position of the RIF peak within the interpolated sub-interval will be at most δ_v. If the distribution of the peak position is uniform within the sub-interval, then the average error is

$$\overline{\varepsilon}_i = \frac{1}{2}\overline{v}\,\tau_A = \frac{\overline{v}}{2 f_A} \tag{5}$$

where f_A is the average sample rate of the accelerometer in hertz. Therefore, the error variance $\sigma_{\varepsilon i}^2$ is

$$\sigma_{\varepsilon i}^2 = \left(\frac{\partial \overline{\varepsilon}_i}{\partial \overline{v}} \sigma_v \right)^2 + \left(\frac{\partial \overline{\varepsilon}_i}{\partial f_A} \sigma_{fA} \right)^2 + 2 \cdot \mathrm{cov}[\overline{v}, f_A] = \left(\frac{1}{2 f_A} \sigma_v \right)^2 + \left(\frac{\overline{v}}{2 f_A^2} \sigma_{fA} \right)^2 \tag{6}$$

where σ_v and σ_{fA} are the standard deviations of the vehicle speed and accelerometer sample rate respectively. The covariance factors are zero because the accelerometer sample rate is independent of the vehicle's speed.

Transient response distance

The sprung and unsprung mass of typical vehicle suspension systems produces their characteristic body- and axle-bounces respectively. Hence, the transient response distance will be in a position ahead of the peak where the total vertical acceleration energy has accumulated to within 1% of its final value. Based on previous work by the author (Bridgelall 2014), Fig 2 shows the vertical acceleration of the impulse response from a quarter-car suspension with the parameters listed in Table 1. The decay envelope and the accumulated accelerometer signal energy from body bounce asymptotically approach their final values after about 4 seconds. The signal energy accumulates to approximately 99% of its final value at three time-constants of the longest lasting oscillations, which is the decaying body bounce. One time constant $\tau_{c\mu}$ is the average duration for the body bounce to decay by a factor of e^{-1} of its initial envelope amplitude. The decay envelope $G_e(t)$ is derived by taking the second derivative of the sprung mass impulse response (Bridgelall 2014) to yield

$$G_e(t) = \omega_{\mu s} \exp\left(-\zeta_{\mu s}\omega_{\mu s} t\right) \tag{7}$$

where $\omega_{\mu s}$ and $\zeta_{\mu s}$ are the mean values of the sprung mass resonance frequency and damping ratios respectively. Solving for t when $G_e(t) = G_e(0)\cdot e^{-1}$ gives the average time constant $\tau_{c\mu}$ as

$$\tau_{c\mu} = \frac{1}{\zeta_{\mu s}\omega_{\mu s}} \tag{8}$$

Hence, the average transient response distance $\bar{\varepsilon}_d$ is

$$\bar{\varepsilon}_d = 3\tau_{c\mu}\bar{v} \tag{9}$$

The average frequency responses of the accelerometer signal provides an estimate for the parameters $\omega_{\mu s}$ and $\zeta_{\mu s}$ as described in previous work (Bridgelall 2014). Fig 3 plots the body bounce and corresponding vertical acceleration from traveling over a simulated bump at 2.5 m·s^{-1}. Table 2 summarizes the vehicle and sensor parameters for the simulation. Fig 4 compares the resulting frequency responses from a single- and a double-axle traversal. The latter produces the energy harmonics indicated because of the semi-periodic nature of the response.

The variance of the transient response distance $\sigma^2_{\varepsilon d}$ is

$$\sigma^2_{\varepsilon d} = \left(\frac{\partial \bar{\varepsilon}_d}{\partial \bar{v}}\sigma_v\right)^2 + \left(\frac{\partial \bar{\varepsilon}_d}{\partial \zeta_{\mu s}}\sigma_{\zeta s}\right)^2 + \left(\frac{\partial \bar{\varepsilon}_d}{\partial \omega_{\mu s}}\sigma_{\omega s}\right)^2 + 2\cdot\mathrm{cov}\left[\bar{v}, \zeta_{\mu s}, \omega_{\mu s}\right] \tag{10}$$

where $\sigma_{\zeta s}$, and $\sigma_{\omega s}$ are the standard deviations of the sprung mass damping ratio and resonance frequency respectively. The last term of equation (10) contains the covariance factors. These are independent parameters when the suspension system operates normally, hence the covariance factor must be zero. After evaluating the partial derivatives equation (10) becomes

$$\sigma^2_{\varepsilon d} = \left(\frac{3}{\zeta_{\mu s}\omega_{\mu s}}\sigma_v\right)^2 + \left(\frac{3\bar{v}}{\zeta_{\mu s}\omega^2_{\mu s}}\sigma_{\zeta s}\right)^2 + \left(\frac{3\bar{v}}{\zeta^2_{\mu s}\omega_{\mu s}}\sigma_{\omega s}\right)^2 \tag{11}$$

As observed and expected the transient response variance increases as the average speed increases.

Sensor position

The sensor position is relative to the first axle that crosses the bump. Hence, distances behind the first axle are negative with respect to the velocity vector. When using smartphones, they will likely be located within arm's length of the driver. For example, with an average arm span of 1.5

meters and an average operator position of 2 meters behind the first axle, the sensor's lateral position could range from -0.5 to -3.5 meters. For a normal distribution, the average distance $\bar{\varepsilon}_s$ will be negative two meters with a standard deviation $\sigma_{\varepsilon s}$ of 1.5/3.0 = 0.5 meters.

GPS tagging error

The GPS position tag $\bar{\varepsilon}_{GPS}$ reported by the sensor operating system consists of two bias components where the average position is

$$\bar{\varepsilon}_{GPS} = \bar{\varepsilon}_{pGPS} + \bar{\varepsilon}_{\tau GPS} \tag{12}$$

Typically the GPS geospatial position error ε_{pGPS} is normally distributed with zero mean, hence $\bar{\varepsilon}_{pGPS} = 0$. This error comes from variances in atmospheric effects, line-of-sight conditions, and GPS receiver quality (Gade 2010). GPS system administrators expect that the 95% confidence interval for horizontal position accuracy, under direct line-of-sight conditions, will be about 6.7 meters. However, this uncertainty could increase to more than 10 meters when large trees and multi-path reflections from buildings and other tall structures distort faint satellite signals.

The literature seldom addresses the second bias component $\bar{\varepsilon}_{\tau GPS}$, which comes from sensor latencies in computing and reporting the geospatial coordinates. The typical modern GPS receiver is an embedded module within another electronic device such as a smartphone or a vehicle circuit board. The GPS module computes a geospatial coordinate at regular update intervals and stores the last update in an output register. A host operating system retrieves the last coordinate from the register via a serial bus interface, formats it, and transfers it to the higher-level software application that requests it. The typical sensor fusion application tags these coordinates with the system time-stamp, and appends them to the signal samples from other embedded sensors, for example, accelerometers and gyroscopes. Depending on the computing platform, the delay in preparing, retrieving, and reporting the geospatial coordinates via the software application stack can be several seconds. Consequently, the geospatial position tags for the accelerometer data stream of a moving vehicle will lag the position of the actual event. The average GPS tag distance lag $\bar{\varepsilon}_{\tau GPS}$ is

$$\bar{\varepsilon}_{\tau GPS} = \bar{\tau}_{lag} \bar{v} \tag{13}$$

where $\bar{\tau}_{lag}$ is the average fetch-to-tag latency. From Equation (12), the total geospatial position tagging variance σ_{GPS}^2 is

$$\sigma_{GPS}^2 = \sigma_{pGPS}^2 + \sigma_{\tau GPS}^2 \tag{14}$$

where σ_{pGPS}^2 is the geospatial position variance and the tag lag variance $\sigma_{\tau GPS}^2$ is

$$\sigma_{\tau GPS}^2 = \left(\bar{v}\sigma_{\tau lag}\right)^2 + \left(\bar{\tau}_{lag}\sigma_v\right)^2 \tag{15}$$

The lag time standard deviation $\sigma_{\tau lag}$ has two components. The first is from variations between the time to fetch the coordinates from the GPS module and the time to tag the accelerometer samples with the system clock. The second is from variations in coordinate "freshness" which is the time difference between computing the GPS coordinates of the instantaneous vehicle position and retrieving the coordinates from the output register. For relatively few task threads or dedicated sensors with few interrupts, the fetch-to-tag time variance is likely negligible. However, the coordinate freshness will vary randomly because the application layer tasks and the GPS receiver updates are asynchronous. For a normally distributed coordinate freshness, the standard deviation will be approximately one-sixth of the GPS update interval $T_{\mu GPS}$ where

$$\sigma_{\tau lag} \cong T_{\mu GPS} / 6 \tag{16}$$

That is, the tag lag standard deviation is essentially the freshness standard deviation because it is the dominant factor.

Precision bounds of position estimate

Rearranging the parameters of Equation (3) produces the position error $\tilde{\upsilon}$ which is a random variable where

$$\tilde{\upsilon} = \breve{\upsilon}_p - \upsilon_p = \Delta L + \hat{\varepsilon}_d + \hat{\varepsilon}_s + \hat{\varepsilon}_i + \hat{\varepsilon}_{GPS} \tag{17}$$

Hence, the variance of the peak position estimate is the sum of the variances of the four error components where

$$\sigma_\upsilon^2 = \sigma_{\varepsilon d}^2 + \sigma_{\varepsilon s}^2 + \sigma_{\varepsilon i}^2 + \sigma_{GPS}^2 = \sigma_{\varepsilon d}^2 + \sigma_{\varepsilon s}^2 + \sigma_{\varepsilon i}^2 + \left(\sigma_{pGPS}^2 + \sigma_{\tau GPS}^2\right) \tag{18}$$

That is, the resultant variance σ_v^2 of the peak position is the sum of the variances of the transient response distance $\sigma_{\varepsilon d}^2$, the sensor position $\sigma_{\varepsilon s}^2$, the digital peak position $\sigma_{\varepsilon i}^2$, and the overall GPS geospatial variance σ_{GPS}^2. Hence, Equation (18) characterizes the error magnitude of each component that constrains the maximum precision achievable when estimating the position of a bump's peak from the ensemble average RIF.

Case Study

The pavement features selected to produce RIF peaks were a speed bump on a park road, an uneven asphalt-concrete pavement joint on an airport access road, and a rail grade crossing on a local road. Fig 5 shows the street level views of each anomaly. Each has relatively smooth adjacent segments to produce discernible RIF peaks. The park bump experiment used a Ford Explorer 2001 sports utility vehicle (SUV) to collect three sets of data at different speeds. The airport access road experiments used a 2007 Subaru Legacy sedan to collect eastbound (EB) and westbound (WB) data sets. The rail grade crossing experiments used the sedan to collect data. An iOS® application (app) logged the GPS and accelerometer data for all traversals. Each vehicle completed 30 traversals across the rough spots of each road segment and maintained the average speed indicated in the header of Table 3. The ensemble average RIF excluded one outlier for each data set.

Anomaly position estimate

The charts on the left side of Fig 6 shows the ensemble average RIF for the six case studies and a Gaussian fit of the RIF distribution between the *a* and *z* vertical markers shown. The distance indicated on the horizontal axis of each graph is relative to the geospatial coordinates of a known position marker on the traversal path. The position of the first peak in the distribution estimates the position of the first axle crossing. When the second peak is detectable, such as for the 5 $m{\cdot}s^{-1}$ case, it estimates the position of the rear axle crossing.

The last row of Table 3 summarizes the resultant error in estimating the position of the true peak for each case study. The average resultant error for all cases was -2.6 meters. For these cases, the individual error components are quantifiable because of the known positions of the sensors and the bumps. Table 3 summarizes the expected biases for ΔL, $\bar{\varepsilon}_s$, $\bar{\varepsilon}_i$, $\bar{\varepsilon}_d$, and $\bar{\varepsilon}_{GPS}$ and the associated parameters needed to calculate their values based on the models developed. It is evident that the transient response and the GPS tag lag errors are in opposite directions. Therefore, they tend to cancel such that the resultant error is much smaller and well within the ranges anticipated for only 30 traversals.

The experiments also validated that the vehicle dashboard was the most convenient spot to attach the smartphone data logger because that position provided the best satellite line-of-sight conditions for reliable GPS receiver updates. Hence, the devices were at a lateral distance of 92 and 71 centimeters behind the axles of the SUV and the sedan respectively. Substituting the average traversal speed $\bar{v}$ and the average sample rate of the accelerometer f_A into Equation (5) produced the $\bar{\varepsilon}_i$ values. Similarly, substituting their mean and standard deviations into Equation (6) produced the standard deviations of the distance interpolation errors. As expected, the interpolation errors were negligible when compared with other error components.

From Equations (8) and (9), the mean sprung mass resonance frequency $\omega_{\mu s}$ and the mean damping ratio $\zeta_{\mu s}$ determines the mean transient response distance $\bar{\varepsilon}_d$. Fig 7 plots the ensemble average from traversing the speed bump at 2.5 m·s^{-1}. A least squares fit of the combined sensor and quarter-car frequency responses with the ensemble average of the Discrete Fourier Transforms (DFT) of the vertical acceleration signal samples $\{g_z\}$ from each traversal produced the estimated suspension parameters listed in Table 1. Similarities with the simulation results shown in Fig 4 provide confidence that the models provide adequate characterization of the vehicle's response, including the harmonics produced from the two-axle crossings. The average transient response distance for all case studies was about 11.2 meters. Accounting for the average speeds, the vibration energy from the last axle crossing lasted for an average of about two seconds. This is consistent with the model simulation results shown in Fig 2 and Fig 3.

The expected value of the geospatial position offset from the GPS receiver $\bar{\varepsilon}_{GPS}$ is zero. Hence, the expected GPS position tagging bias depended primarily on the average GPS tag lag distance $\bar{\varepsilon}_{\tau GPS}$. This parameter would be difficult to obtain in general because of the variety of sensors, sample rates, and operating system performances anticipated. However, for these case studies, the lag time statistics are derivable because the error of peak position estimate $\tilde{\upsilon}$ is a known quantity. Taking the expected values of the random variables in Equation (17) and rearranging terms to derive the unknown value yields

$$\bar{\varepsilon}_{\tau GPS} = \tilde{\upsilon} - \left(\Delta L + \bar{\varepsilon}_s + \bar{\varepsilon}_i + \bar{\varepsilon}_d\right) \tag{19}$$

Given the average traversal speed $\bar{v}$, Equation (13) produces the average tag lag $\bar{\tau}_{lag}$ that Table 3 summarizes for each case study. The average tag lag time and the equivalent average distance for the case studies was about -2.3 seconds and -14 meters, respectively.

Relative error magnitudes

Table 3 includes the mean and standard deviations of parameters needed to compute the position error magnitude for each case study. As indicated, the standard deviation of peak position estimation within the interpolated sub-intervals $\sigma_{\varepsilon i}$ was negligible. From Equation (6), the average uncertainty across all case studies was only 2 millimeters. The variance of sensor position $\sigma^2_{\varepsilon s}$ was zero for each case study because their fixed position in each vehicle. Equation (11) provides the average uncertainty in transient response distance $\sigma_{\varepsilon d}$ where the average of the standard deviations across all case studies was about 0.7 meters.

From Equation (16), the tag lag standard deviation was about 0.2 seconds because the average GPS update period was one approximately second. From Equation (15) the average tag lag uncertainty $\sigma_{\tau GPS}$ was about 1.3 meters. The GPS position variance σ^2_{pGPS} is derived by solving Equation (18) in terms of the variances that are now known such that

$$\sigma^2_{pGPS} = \sigma^2_{\upsilon} - \left(\sigma^2_{\varepsilon d} + \sigma^2_{\varepsilon s} + \sigma^2_{\varepsilon i} + \sigma^2_{\tau GPS}\right) \tag{20}$$

The data collected and summarized in Table 3 for each case study includes the peak position standard deviation σ_v for the RIF. Hence, the GPS position uncertainty for each case study was as shown in the table, and the average across all data sets was about 3.4 meters. This result is well within the range expected of practical applications that use standard GPS technology. In conclusion, the position uncertainty from the GPS receiver was the dominant factor in the achievable precision of estimating the actual position of the pavement anomaly.

Precision bounds

The (1-α) percent margin-of-error (MOE) of the peak position estimate is denoted $\Delta\varepsilon_{1-\alpha}$ as follows:

$$\Delta\varepsilon_{1-\alpha} = \pm\frac{\sigma_{\upsilon} q_{1-\alpha/2}}{\sqrt{N_{v}}} \tag{21}$$

The standard normal quantile is $q_{1-\alpha/2}$ for a confidence interval of (1-α)%. The number of vehicle traversals is N_v. Hence the 95% confidence interval is $2\Delta\varepsilon_{0.95}$ and $q_{1-\alpha/2} = 1.96$.

The charts on the right side of Fig 6 are histograms of peak RIF positions for each traversal set, and several distribution types that best fit the histograms in the least squares sense. Table 4 lists the distribution parameters and chi-squared values indicating their respective goodness-of-fit. For all the cases, the chi-squared significance levels are not sufficiently small to reject any of the hypothesized distributions indicated. The table indicates the largest significance levels for each case in bold font. Hence, the Logistic distribution appears to describe the spread of the RIF peak best for the speed bump case studies whereas the Gaussian and Student's t-distributions appear to provide a better fit for the remaining cases. However, the Logistics distribution provides chi-squared significance levels that are similar to those of the Gaussian and Student's t-distributions. Among the distributions hypothesized, the Weibull provides the smallest significance levels. Hence, the data appears to follow classic distributions where the distribution means are the best estimators for the actual position of the anomaly, and their standard deviations provide the confidence intervals.

The MOE diminishes with increasing traversal volume in the manner described by Equation (21). Fig 8 compares the MOE for the 2.5 m·s^{-1} speed bump case study with a typical scenario (Gillespie 2004) consisting of vehicles with the parameters summarized in Table 5. For a maximum deviation of the GPS position estimate of 30 meters, the standard deviation would be 10 meters. The typical scenario includes vehicle traversals that are within one standard deviation equal to 10% of the average vehicle speed. Therefore, the precision bound for a larger vehicle volume is expectedly greater because of the broader parameter spread. For example, about 10 traversals provided a peak position estimate within 3 meters with 95% confidence for the case study vehicles whereas 45 traversals will be required to achieve similar results with a typical vehicle mix. With the parameter variances provided, the precision improves rapidly as the volume grows beyond 10 vehicles while volumes beyond 50 vehicles provide diminishing returns.

Error sensitivity

Table 6 summarizes the sensitivities of bias errors to vehicle and sensor parameters. The cells associated with the partial derivatives indicated in their columns and rows are the error rates associated with the mean values shown in column seven. For example, the transient response distance error $\bar{\varepsilon}_d$ is sensitive to velocity changes at the rate of $\partial\bar{\varepsilon}_d / \partial\bar{v} = 2.62$ seconds. The total velocity sensitive error rate is 5.13 seconds. Hence, the sensitivity for this bias component is about 12.82 meters for a 100% change in the mean velocity of 2.5 m·s^{-1}. The product of the rates and the mean parameter values normalizes all results to units of distance for comparison. These would be the biases produced by the individual error components if the vehicle and sensor parameters deviate 100% from their mean values. Hence, variances in vehicle suspension damping ratios and speed are the two dominant error components. As noted, variances in GPS tagging also produce significant bias errors.

Summary and Conclusions

The emergence of connected vehicles and smartphones as distributed sensors offer lucrative opportunities to reduce significantly the cost of continuous, network-wide pavement performance monitoring. As a multi-resolution filter, the RIF transform summarizes pavement ride-quality in direct proportion to the IRI. The RIF transform also provides a suitable method of aggregating voluminous data from GPS and inertial sensors on board vehicles to locate potential pavement distress symptoms, some of which could lead to catastrophic events and damages. This study characterizes bounds in the precision of a RIF position estimator as a function of traversal volume and variances in sensor and vehicle parameters. Six case studies demonstrated that vehicle suspension transient motion and the average GPS sensor latency are the dominant errors in the estimating the position of anomalies. Similarly, the case studies found that variance in GPS position tagging was the largest factor limiting precision in peak position estimation. Nevertheless, estimation precision improves with vehicle traversal volume, making this approach attractive for deployment in a connected vehicle environment. For a typical vehicle mix, the precision improves substantially as traversals approach 50.

Future work will characterize the severity and dimensions of potential distress symptoms from RIF signatures. RIF shapes shows promise in providing a suitable feature for anomaly classification to differentiate between rough spots produced from known features such as manhole covers, and unwanted distress symptoms, such as potholes and frost heaves.

Acknowledgement

A grant from the Mountain Plains Consortium supported this research.

Notation

This paper uses the following symbols:

f	=	frequency in hertz;
$g_z(t)$	=	vertical g-force output from the inertial sensor as a function of time t;
ΔL	=	length of road segment;
N_v	=	the traversal volume;
$R_{\bar{v}}^{\Delta L}$	=	RIF for segment of length ΔL at average speed $\bar{v}$;
$\overline{R}^{\Delta w}(x)$	=	the ensemble average RIF across spatial window size Δw at distance x;
$q_{1-\alpha/2}$	=	the standard normal quantile for a (1-α)% confidence interval;
$v(t)$	=	instantaneous traversal speed as a function of time;
$\bar{v}$	=	average traversal speed;
$\Delta\varepsilon_{1-\alpha}$	=	the (1-α)% margin-of-error;
$\bar{\varepsilon}_d$	=	average suspension system transient response distance;
$\bar{\varepsilon}_{GPS}$	=	average GPS position bias;
$\bar{\varepsilon}_{pGPS}$	=	average GPS geo-spatial position error;
$\bar{\varepsilon}_{\tau GPS}$	=	average GPS tag lag from operating system latency;
$\bar{\varepsilon}_i$	=	average peak position error within the distance interpolation sub-interval;
$\bar{\varepsilon}_s$	=	average longitudinal sensor position behind the first axle;
γ_z	=	accelerometer (sensor) constant;

κ_{RI}	=	proportionality constant of the RIF/IRI impulse response ratio;
$\tilde{\upsilon}$	=	error between the estimate and the true position;
υ_p	=	actual position of a feature on the road that produces the RIF peak;
$\check{\upsilon}_p$	=	position of a peak in the ensemble RIF;
ω_{Gs}	=	Golden Car sprung mass angular resonance frequency;
ω_{Gu}	=	Golden Car unsprung mass angular resonance frequency;
$\omega_{\mu s}$	=	average sprung mass angular resonance frequency;
$\omega_{\mu u}$	=	average unsprung mass angular resonance frequency;
ρ_z	=	ratio of average unsprung to sprung mass coefficient;
$\sigma_{\varepsilon s}$	=	standard deviation of the sensor's lateral position relative to the first axle;
$\sigma^2_{\varepsilon d}$	=	variance of the transient response distance;
$\sigma^2_{\varepsilon i}$	=	variance of the digital peak position;
$\sigma^2_{\varepsilon s}$	=	variance of the sensor position;
$\sigma_{\varepsilon s}$	=	standard deviation of the sensor's lateral position relative to the first axle;
σ^2_{GPS}	=	total position tagging variance;
σ^2_{υ}	=	resultant peak position variance;
σ^2_{pGPS}	=	geospatial position variance;
$\sigma^2_{\tau GPS}$	=	GPS tag lag variance;
σ_v	=	standard deviation of the vehicle speed;
σ_{fA}	=	standard deviation of the accelerometer sample rate;
$\sigma_{\omega s}$	=	standard deviation of the sprung mass resonant frequency;
$\sigma_{\zeta s}$	=	standard deviation of the sprung mass damping ratio;
$\bar{\tau}_{lag}$	=	average operating system latency in fetching and applying GPS tags;

ζ_{Gs}	=	damping ratio of the Golden Car sprung mass frequency response;
$\zeta_{\mu s}$	=	damping ratio of the average sprung mass frequency response;
ζ_{Gu}	=	damping ratio of the Golden Car unsprung mass frequency response;
$\zeta_{\mu u}$	=	damping ratio of the average unsprung mass frequency response.

References

AASHTO. (2009). *Rough Roads Ahead: Fix Them Now or Pay for It Later.* Washington, DC: American Association of State Highway and Transportation Officials (AASHTO) and The Road Information Program (TRIP).

Bridgelall, R. (2014). "Connected Vehicle Approach for Pavement Roughness Evaluation." *Journal of Infrastructure Systems* (American Society of Civil Engineers) 20, no. 1: 04013001.

Bridgelall, R. (2014). "A participatory sensing approach to characterize ride quality." *Proceedings of SPIE Volume 9061, Sensors and Smart Structures Technologies for Civil, Mechanical, and Aerospace Systems.* San Diego: SPIE.

Chen, K., Zhang, X., and Lu, M. (2011). *Data mining system for road pothole detection with on-board sensors.* Bulletin of advanced research, Shenzhen, China: Shenzhen Institutes of Advanced Technology.

Dawkins, J., Bevly, D., Powell, B., and Bishop, R. (2011). *Investigation of Pavement Maintenance Applications of Intellidrive.* Virginia: University of Virginia: DOT Pooled Fund Study.

Eriksson, J., Girod, L., Hull, B., Newton, R., Madden, S., and Balakrishnan, H. (2008). "The pothole patrol: using a mobile sensor network for road surface monitoring." *Proceedings of* *the 6th international conference on Mobile systems, applications, and services.* New York: Association for Computing Machinery (ACM), 29-39.

Federal Highway Administration and Federal Transit Administration (2011). *2010 Status of the Nation's Highways, Bridges, and Transit: Conditions & Performance.* Report to Congress, Washington, DC: U.S. Department of Transportation.

Gade, K. (2010). "A Non-singular Horizontal Position Representation." *The Journal of Navigation* (The Royal Institute of Navigation) 63, no. 3: 365-417.

Gillespie, T. D. (2004). *CarSim Data Manual.* Ann Arbor, Michigan: Mechanical Simulation Corporation.

Griffin, M. J. (1990). *Handbook of Human Vibration.* New York: Elsevier.

Hautakangas, H., and Nieminen, J. (2011). *Data mining for pothole detection.* Pro Gradu Seminar, Finland: University of Jyväskylä.

Hesami, R., and McManus, K. J. (2009). "Signal Processing Approach to Road Roughness Analysis and Measurement." *TENCON 2009 -- IEEE Region 10 Conference.* Swinburn University of Technology, 1-6.

HPMS. (2012). Highway Performance Monitoring System Field Manual (HPMS), Office of Highway Policy Information Federal Highway Administration, Washington, DC: Federal Highway Administration.

Mohan, P., Padmanabhan, V. N., and Ramjee, R. (2008). "Nericell: Rich Monitoring of Road and Traffic Conditions using Mobile Smartphones." *Proceedings of the 6th ACM conference on Embedded network sensor systems - SenSys '08.* Bangalore, India: Microsoft Research India, 323.

Park, K., Thomas, N. and Lee, K.W. (2007). "Applicability of the International Roughness Index as a Predictor of Asphalt Pavement Condition." *ASCE Journal of Transportation Engineering*, 133, No. 12: 706 - 709.

Swedish National Road and Transport Research Institute. (2004). "The influence of road surface condition on traffic safety and ride comfort." *Sixth International Conference on Managing Pavements: The Lessons, The Challenges, The Way Ahead.* Brisbane, Queensland, Australia: Queensland Department of Main Roads.

Zaniewski, J. P., and Butler, B. C. (1985). "Vehicle Operating Costs Related to Operating Mode, Road Design, and Pavement Condition." In *Measuring Road Roughness and Its Effects on User Cost and Comfort*, edited by Thomas D. Gillespie and Michael Sayer, 127-142. Philadelphia: American Society for Testing and Materials.

Table 1: Quarter-car suspension parameters for the speed bump simulation

Parameter	Units	Sprung Mass	Unsprung Mass
Resonant frequency (*f*)	hertz	1.4	12.04
Damping Ratio (ζ)	-	0.13	0.22

Table 2: Vehicle and bump parameters for the simulations

Parameter	Units	Value
Axle separation	m	2.83
Traversal speed	$m \cdot s^{-1}$	2.24
First bump height	cm	5
Second bump height	cm	4
Bump width	cm	30

Table 3: Parameters derived from the data of the six case studies

Parameter	**Speed Bump NB**			**Rd. Bump EB**	**Rd. Bump WB**	**Rail Tracks NB**
	2.5 m·s^{-1}	**5 m·s^{-1}**	**7 m·s^{-1}**	**7 m·s^{-1}**	**7 m·s^{-1}**	**7 m·s^{-1}**
Speed, σ_v (m·s^{-1})	0.208	0.561	0.458	0.420	0.255	0.415
G_z sample rate, f_A (Hz)	93.233	93.283	93.340	93.174	93.207	92.664
G_z sample rate, σ_{fA} (Hz)	0.099	0.074	0.099	0.076	0.116	0.077
Signal peak position, $\overline{\varepsilon_i}$ (m)	0.014	0.027	0.039	0.036	0.036	0.036
Signal peak position, $\sigma_{\varepsilon i}$ (m)	0.001	0.003	0.002	0.002	0.001	0.002
Sensor offset, $\overline{\varepsilon_s}$ (m)	-0.920	-0.920	-0.920	-0.710	-0.710	-0.710
Damping Estimate, $\zeta_{\mu s}$	0.13	0.20	0.20	0.10	0.10	0.10
Sprung Mass Res., $f_{\mu s}$ (Hz)	1.4	1.93	2.48	2.155	2.155	1.8
Transient dist., $\overline{\varepsilon_d}$ (m)	6.669	6.154	6.952	15.019	14.764	17.673
Transient dist., $\sigma_{\varepsilon d}$ (m)	0.544	0.694	0.441	0.931	0.564	1.101
OS lag, $\overline{\tau_{lag}}$ (s)	-1.854	-1.650	-1.083	-3.102	-2.652	-3.722
OS lag, $\sigma_{\tau lag}$ (s)	0.168	0.167	0.166	0.164	0.165	0.169
GPS tag lag, $\overline{\varepsilon_{GPS}}$ (m)	-4.713	-8.211	-7.820	-21.025	-17.669	-24.799
GPS tag lag, $\sigma_{\tau GPS}$ (m)	0.575	1.245	1.294	1.714	1.289	1.911
RIF Peak Position, $\breve{\upsilon}$ (m)	32.200	28.200	29.400	24.600	27.700	25.300
RIF Peak Position, σ_{υ} (m)	4.973	5.125	3.755	2.072	3.527	3.595
GPS position error, σ_{pGPS}	**4.904**	**4.923**	**3.497**	**0.701**	**3.234**	**2.839**
RIF Peak offset, $\tilde{\upsilon}$ (m)	2.050	-1.950	-0.750	-5.680	-2.580	-6.800

Table 4: Estimated distributions of the peak RIF position for each case study

Parameter	Speed Bump NB 2.5 $m \cdot s^{-1}$	Speed Bump NB 5 $m \cdot s^{-1}$	Speed Bump NB 7 $m \cdot s^{-1}$	Rd. Bump EB 7 $m \cdot s^{-1}$	Rd. Bump WB 7 $m \cdot s^{-1}$	Rail Tracks NB 7 $m \cdot s^{-1}$
Gaussian						
df	17	17	15	6	13	17
χ^2 (α = 5%)	27.587	27.587	24.996	12.592	22.362	27.587
χ^2 Data	14.854	18.738	18.772	2.887	11.322	26.044
Data Sig. α (%)	*60.597*	*34.379*	*22.426*	***82.286***	*58.384*	***7.367***
Amplitude	62.100	43.646	28.400	33.528	31.310	29.630
Mean	35.446	30.541	27.524	27.086	25.822	26.381
Standard Dev.	9.369	8.665	3.619	2.960	4.468	3.515
Student-t						
df	17	17	15	6	13	17
χ^2 (α = 5%)	27.587	27.587	24.996	12.592	22.362	27.587
χ^2 Data	14.795	18.425	18.575	2.908	11.082	26.094
Data Sig. α (%)	*61.026*	*36.254*	*23.365*	*82.024*	***60.398***	*7.276*
Amplitude	59.685	44.091	28.897	36.051	32.233	30.174
Mean	34.860	30.448	27.488	27.144	25.805	26.356
Standard Dev.	8.965	8.585	3.584	3.042	4.494	3.528
Logistic						
df	17	17	15	6	13	17
χ^2 (α = 5%)	27.587	27.587	24.996	12.592	22.362	27.587
χ^2 Data	14.523	18.042	14.675	3.025	11.452	26.068
Data Sig. α (%)	***62.980***	***38.619***	***47.506***	*80.567*	*57.298*	*7.323*
Amplitude	56.884	45.022	29.663	35.912	33.256	31.035
Mean	34.113	30.328	27.451	27.151	25.777	26.296
Scale	5.489	5.528	2.319	1.978	2.950	2.304
Weibull						
df	17	17	15	6	13	17
χ^2 (α = 5%)	27.587	27.587	24.996	12.592	22.362	27.587
χ^2 Data	17.940	20.801	16.130	4.279	14.224	30.731
Data Sig. α (%)	*39.264*	*23.534*	*37.343*	*63.895*	*35.825*	*2.153*
Amplitude	48.700	48.500	50.000	33.169	30.075	50.000
Shape (k)	1.900	1.600	2.000	1.637	2.161	2.100
Scale (α)	18.400	14.500	13.200	5.877	9.745	14.000

Table 5: Vehicle parameters to compare precision bounds

Parameter	Units	Typical	Case I
GPS estimate (standard deviation)	m	10	4.904
Sensor position (standard deviation)	m	0.5	0
Vehicle speed (average)	$m \cdot s^{-1}$	2.50	2.542
Speed (standard deviation)	$m \cdot s^{-1}$	0.254 (10%)	0.208 (8.1%)
Body bounce resonance (average)	hertz	1.2	1.4
Body bounce resonance (standard deviation)	hertz	0.1	0
Damping ratio (average)	-	0.35	0.13
Damping ratio (standard deviation)	-	0.02	0

Table 6: Average position error sensitivity with typical values for each error rate and parameter

Error Rate	$\partial\overline{\varepsilon_i}$	$\partial\overline{\varepsilon_d}$	$\partial\overline{\varepsilon_{\tau GPS}}$	$\partial\overline{\varepsilon_s}$	**Total Rate**	**Mean Value**	**Sensitivity (Meters)**
$\partial\bar{v}$	5.36×10^{-3}	2.62	-2.50	0	5.13 s	2.5 $m\cdot s^{-1}$	12.82
$\partial\omega_{\mu s}$	0	0.76	0	0	0.76 $m\cdot rad^{-1}$	7.54 rad	5.72
$\partial\zeta_{\mu s}$	0	51.3	0	0	51.3 m	0.35	17.96
∂f_A	3.1×10^{-4}	0	0	0	3.1×10^{-4} $m\cdot Hz^{-1}$	64 Hz	0.02
$\partial\overline{\tau_{lag}}$	0	0	2.54	0	2.54 $m\cdot s^{-1}$	-2.50 s	-6.36
$\partial\overline{\varepsilon_s}$	0	0	0	1.00	1.00	-2.00	-2.00

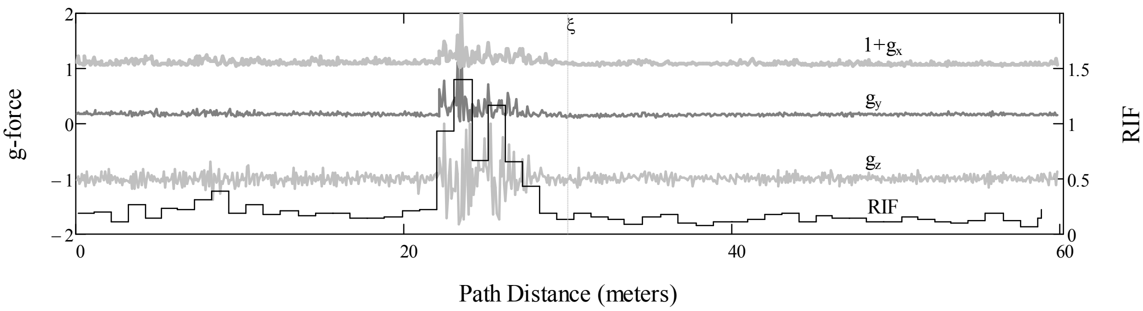

Figure 1. Accelerometer signals and RIF profile from a single traversal of speed bump at 7 $m\cdot s^{-1}$

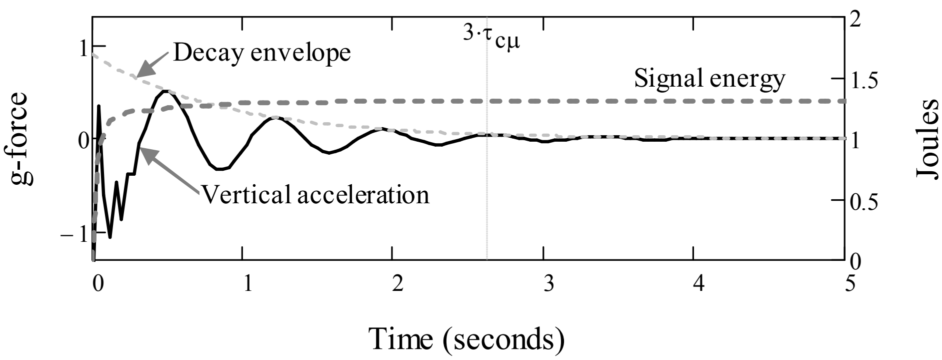

Figure 2. Simulated vertical acceleration of the suspension impulse response and signal energy

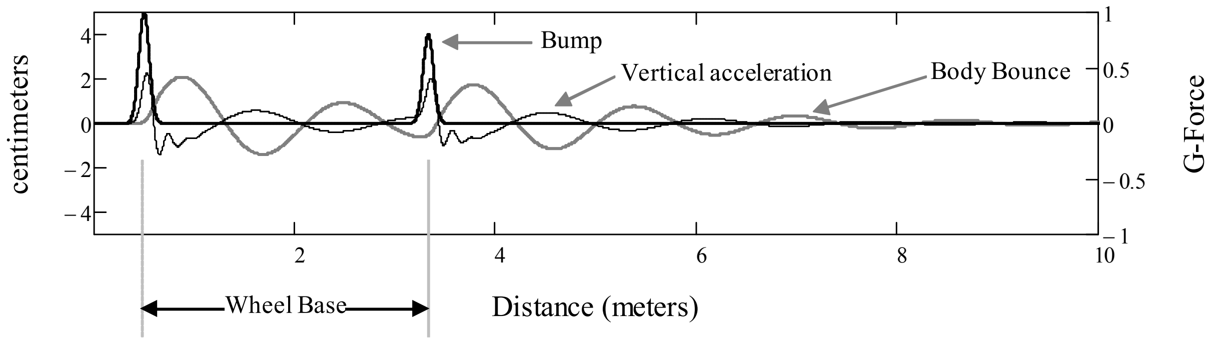

Figure 3. Simulated bump profile, vehicle body bounce response, and accelerometer signal

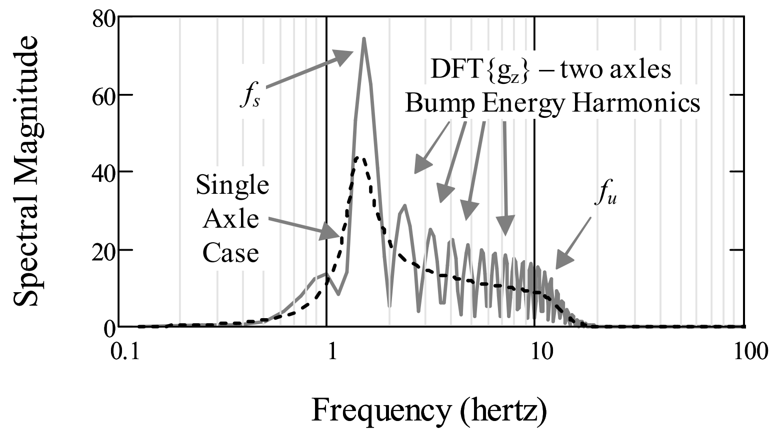

Figure 4. DFT of simulated accelerometer signal for single- and double-axle traversals

Figure 5. Bumps traversed for this case study

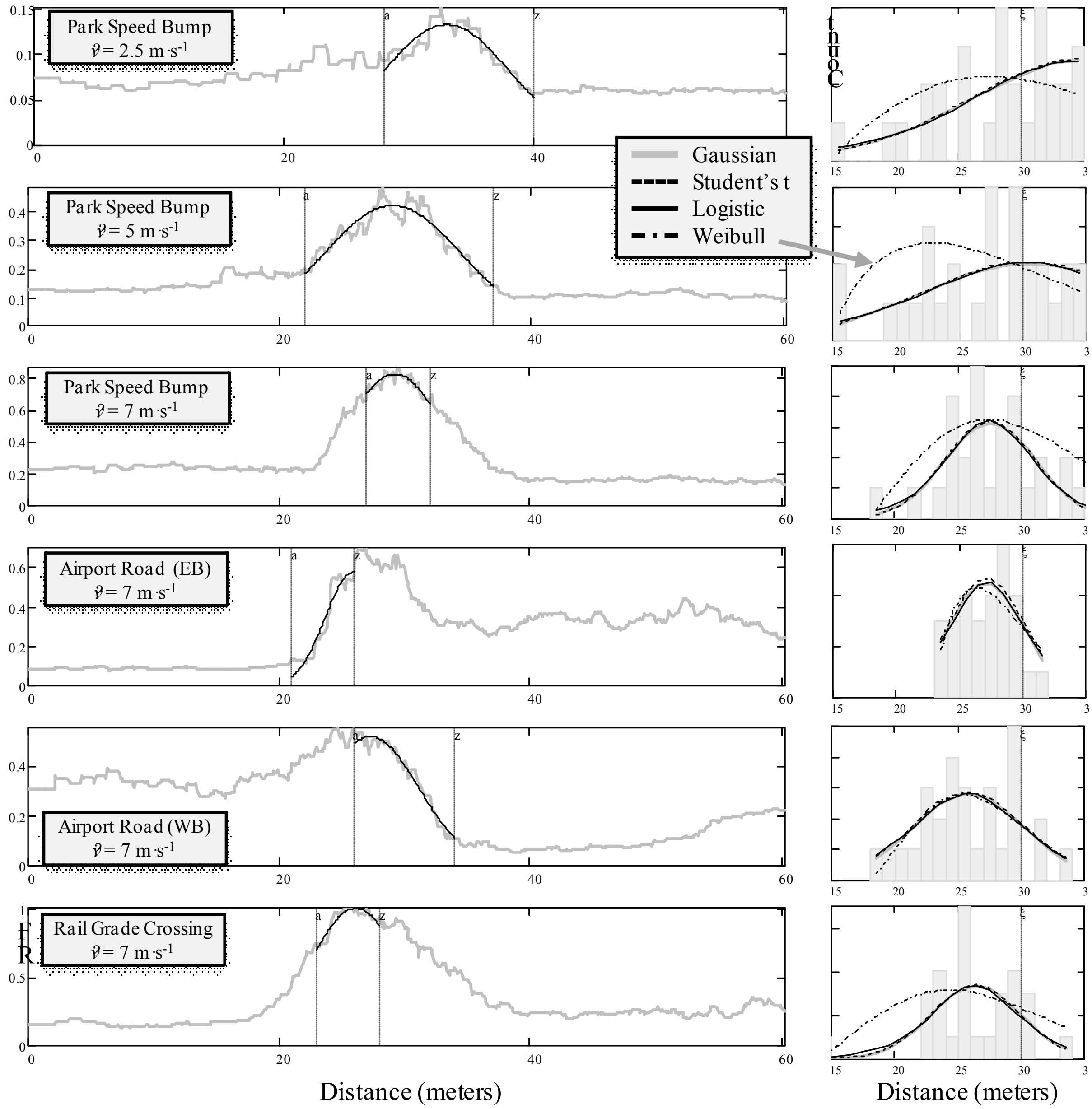

Figure 6. Ensemble average RIF for each case study and the associated distribution of their RIF peak position

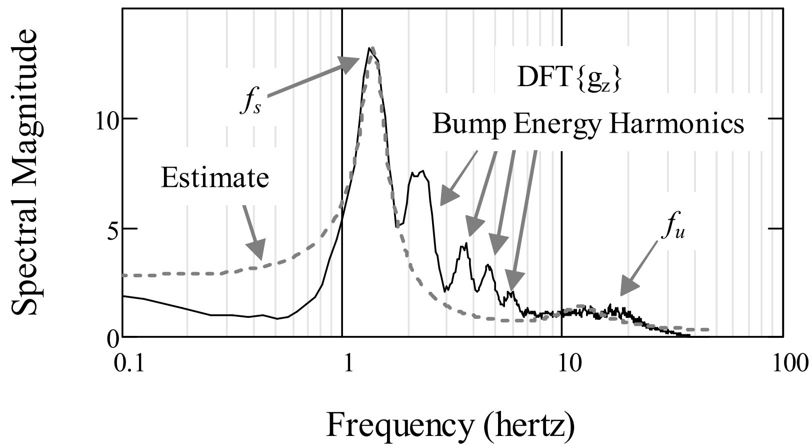

Figure 7. DFT of accelerometer output and an estimate of the equivalent quarter-car response

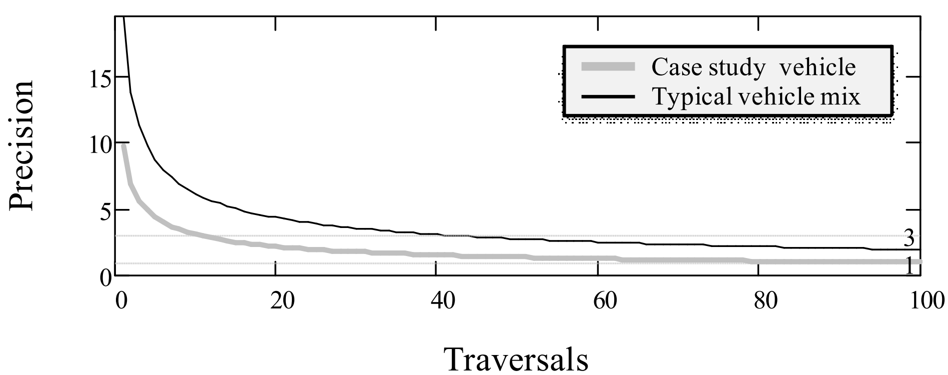

Figure 8. Precision bounds for the speed bump case study vehicle and an expected vehicle mix